Dentate spikes and external control of hippocampal function

Dvorak, D.[1], Chung, A.[1,*], Park E. H.[1], Fenton, A. A.[1,2,3]

[1] Center for Neural Science, New York University, New York, NY

[2] Neuroscience Institute at the NYU Langone Medical Center, New York, NY

[3] The Robert F. Furchgott Center for Neural and Behavioral Science, Dept. of Physiology and Pharmacology, SUNY, Downstate Medical Center, Brooklyn, NY

[*] Massachusetts General Hospital, Boston, MA (current affiliation)

Author for Correspondence:

André Fenton

Center for Neural Science and Neuroscience Institute at the NYU Langone Medical Center

(212) 992 6573

afenton@nyu.edu

Abstract

Mouse hippocampus CA1 place-cell discharge typically encodes current location but during slow gamma dominance (SG_{dom}), when slow gamma oscillations (30-60 Hz) dominate mid-frequency gamma oscillations (60-90 Hz) in CA1 local field potentials, CA1 discharge switches to represent distant recollected locations. We now report that dentate spike type 2 (DS_M) events initiated by MECII→DG inputs promote SG_{dom} and change CA1 discharge, whereas type 1 (DS_L) events initiated by LECII→DG inputs do not. Just before SG_{dom}, LECII-originating slow gamma oscillations in dentate gyrus and CA3-originating slow gamma oscillations in CA1 become optimally phase and frequency synchronized at the DS_M peak when the firing rates of DG, CA3, and CA1 principal cells increase to promote DG→CA3→CA1 cofiring optimized for the 5-10 ms DG-to-CA1 neuro-transmission that coincides with SG_{dom}. Several properties and consequences of DS_M demonstrate extrahippocampal control of SG_{dom}, identifying a cortico-hippocampal mechanism that switches between memory-related hippocampal information processing modes.

Introduction

The hippocampus is critical for long-term memory storage and use, requiring that neural discharge represent both what has occurred and what is happening. How do multifunction neural networks like hippocampus accomplish mutually incompatible tasks like recollecting the past and encoding the present? One possibility is that separate neural circuits operate in parallel to perform each information processing task, but this does not appear to be the case for hippocampus. Rather, in hippocampus the same populations of excitatory and inhibitory neurons are organized such that network discharge patterns, sometimes called cell assemblies (Harris et al., 2003; Hebb, 1949) rapidly switch between different information processing modes, often in a winner-take-all fashion (Colgin, 2015; Kelemen and Fenton, 2010; Kelemen and Fenton, 2013; Kelemen and Fenton, 2016; Papale et al., 2016; Pastalkova et al., 2008; van Dijk and Fenton, 2018; Wu et al., 2017). We reported that position-representing CA1 ensemble spike trains switched between representing the current, local position and distant places, which during an active place avoidance task represented recollected locations of prior shocks (Dvorak et al., 2018). CA1 switched to signaling distant places during slow-gamma dominance (SG_{dom}), which we defined as when slow gamma (30-60 Hz) oscillations dominate mid-frequency (60-90 Hz) gamma oscillations in the CA1 local field potential (LFP; Dvorak et al., 2018). How do such network transitions occur to change information processing?

One way to switch between multiple mutually-exclusive tasks is to organize the network such that its intrinsic excitation-inhibition dynamics transition between the multiple information processing modes with winner-take-all dynamics (de Almeida et al., 2009; Rolls and Treves, 1998). Alternatively, an external control signal can select the information processing mode (Fig. 1A, top). In the intrinsic case, the functional state transitions of the network are either biased by a stronger input, or related to some other internal mechanism (Fig. 1A, middle). In the extrinsic case, distinct control input signals predict the transition into functional states (Fig. 1A, bottom).

We previously observed transient (~500 ms) recollection-associated SG_{dom} events (Figs. 1B-D) at the same rate during free exploration or a memory task (Dvorak et al., 2018), pointing to the possibility that SG_{dom} is unrelated to cognitive demand or environmental variables, and is instead initiated within hippocampus. Here we investigate an alternative, that these SG_{dom} associated switches of the CA1 information processing state are controlled by discrete events in the perforant path tri-synaptic input from the entorhinal cortex.

CA1 slow gamma originates in CA3 (Lasztoczi and Klausberger, 2014, 2016; Schomburg et al., 2014), motivating us to seek evidence of extrahippocampal control signals either directly via the temporoammonic input from entorhinal cortex layer 3 (ECIII) or indirectly from ECII via the perforant path to dentate gyrus (DG). We examined dentate spikes, the under-investigated, large amplitude, short duration field potentials that localize to DG (Figs. 1E, F; Fig. S1). They result from entorhinal activation; dentate spikes disappear after bidirectional removal of entorhinal cortex (Bragin et al., 1995). Two types of dentate spikes were previously identified in rat (Bragin et al., 1995) and mouse (Buzsaki et al., 2003). DS type 1 (DS_L in this study) exhibits a polarity reversal in the outer third of the DG molecular layer at the termination zone of the lateral entorhinal cortex layer 2 (LECII) projection, whereas DS type 2 (DS_M in this study) exhibits a polarity reversal in the middle third of the DG molecular layer at the termination zone of the medial entorhinal cortex layer 2 (MECII) projection (Fig. 1F; Bragin et al., 1995). Similar to sharp-wave ripples (SWR), dentate spikes are synchronized across hemispheres (Bragin et al., 1995; Headley et al., 2017). If DS are related to recollection, like SG_{dom} (Dvorak et al., 2018), they should be related to behavior, but little is known about this relationship. Motivated by the distinctive connectivity underlying the two types of DS (Fig. 1F), the differential roles of LEC in non-spatial information and MEC in spatial information processing (Hargreaves et al., 2005; Knierim et al., 2014), and the limited information about DS events, we examined whether DS_L and/or DS_M switches CA1 into the SG_{dom}-associated mode of information processing.

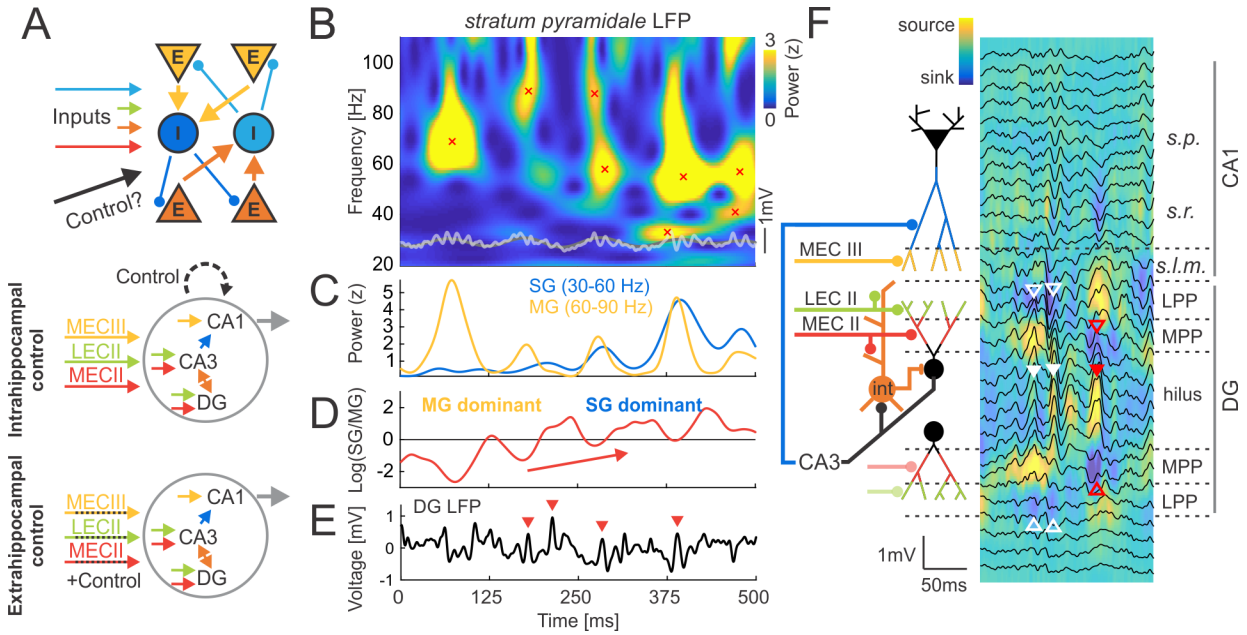

Figure 1. Control of hippocampal activity. A) A network schematic with winner-take-all dynamics, composed of excitatory (E) and inhibitory (I) neurons, excitatory inputs and a possible external control signal (top). Two hypotheses for hippocampal information processing control (middle) intrinsic, intrahippocampal and (bottom) extrinsic, extrahippocampal control. B) Wavelet time-frequency histogram of a 0.5 s CA1 LFP sample (light gray trace) with slow gamma (30-60 Hz) and mid-frequency gamma (60-90Hz) events; theta (5-12 Hz) band-pass filtered LFP shown in dark gray. Red crosses mark local maxima with z-score normalized power > 2.5. C) Concurrent z-score power in the slow (SG: 30-60 Hz) and mid-frequency gamma (MG: 60-90 Hz) bands. D) Concurrent log-transformed SG/MG power ratio illustrates transition from MG dominance (MG_{dom}: log(SG/MG) < 0) to SG dominance (SG_{dom}: log(SG/MG) > 0). E) Concurrent LFP recorded in the hilar region of dentate gyrus (DG) with identified dentate spikes (red arrowheads). F) Two types of dentate spikes can be identified in the DG hilar region. DS_L (full white arrowheads) is identified by a pair of current-source-density (CSD) sinks in the outer molecular layers of DG (empty white arrowheads) at the LECII projection termination. DS_M (full red arrowheads) is identified by a pair of CSD sinks in the middle molecular layers of DG (empty red arrowheads) at the MECII projection termination. Background color represents CSD. Black

traces represent LFP. Simplified circuit schematics (left) illustrating hypothesized components of dentate spike generation and mechanism of CA1 SG_{dom} control.

Results

Identifying DS_L and DS_M events using current source density analysis

We begin by assuming that the two types of dentate spikes can have different functional roles, which requires distinguishing DS_L and DS_M events in the LFPs that we record across the somato-dendritic CA1-DG axis (Fig. 1F; Fig. S2). Putative DS events localize to the hilus. When current source density (CSD) profiles are computed at the DS event peaks, pairs of current sinks localize at both the supra-pyramidal and infra-pyramidal molecular layers of DG (Fig. 1F; Fig. 2A, left). We then identify local minima in the CSD profiles of each putative DS event and compute the histogram along the dorso-ventral axis (Fig. 2A, middle), which reveals a peak concentration of CSD sinks aligned with the visually identified sink regions that correspond to the supraDG and infraDG molecular layers. Putative DS events are classified according to the location of the current sink within the sink histogram. DS_L (DS type 1) sinks are at the outer molecular layers of DG where LECII projections terminate. DS_M (DS type 2) sinks are at the middle molecular layers of DG, where MECII projections terminate. We average the CSDs of DS_L and DS_M events separately for classification using the supraDG and infraDG molecular layers (Fig. 2A, right). This confirms that both types of classification result in events with the same CSD profile, and subsequently we use DS classification according to the presence or absence of a sink at supraDG.

We confirm localization of the outer and middle molecular layers of DG, by electrically stimulating the medial perforant path (MPP) and computing the average CSD of the evoked response (Fig. 2B, right). The evoked response matches the average CSD of DS_M (Fig. 2B, middle), but not DS_L events (Fig. 2B, left), as expected. DS_M (Fig. 2B, middle; T=0 ms) and evoked responses (Fig. 2B, right; T=5 ms) have colocalized pairs of current sinks (white empty

arrowheads in Fig. 2B) in the middle molecular layers of DG, whereas the DS_L sinks are in the outer molecular layers. We are thus confident in identifying distinct DS_L and DS_M events, an advance over prior work.

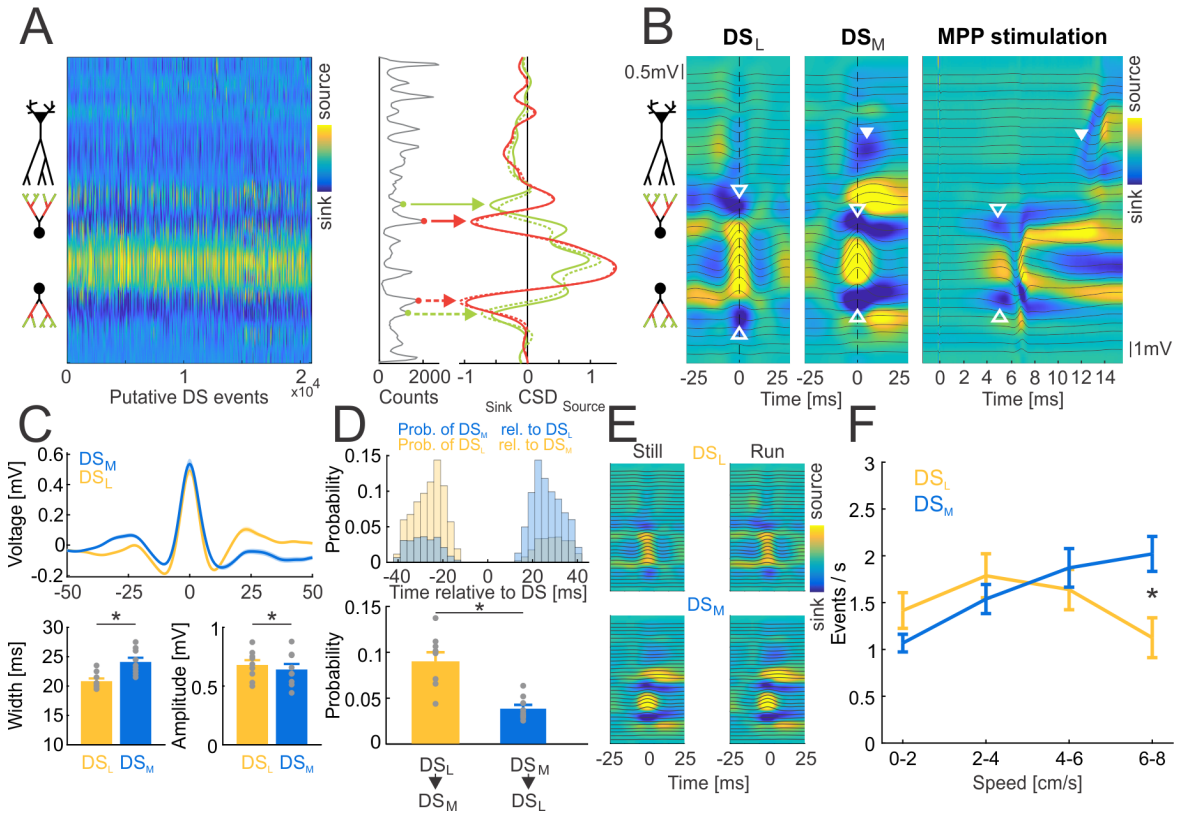

Figure 2. CSD analysis classifies two types of dentate spikes with distinct anatomical, temporal, and behavioral properties. A) CSD of putative DS events (left) shows pairs of sink bands at the outer and middle molecular layers of supraDG and infraDG. Histogram of local minima in CSD profiles (middle) shows peaks aligned with pairs of sink bands in the outer and middle molecular layers. Average CSD profiles (right) of the two types of DS events with CSD minima in the vicinity of the peaks of the CSD minima histograms. Notice the correspondence at the outer molecular layers (supraDG: solid green and infraDG: dashed green traces) and at the middle molecular layers of DG (supraDG; solid red and infraDG: dashed red traces) pointing to the symmetry of the DS-associated CSD sinks. B) Average CSDs of DS_L (left) and DS_M (middle). Notice sinks (white empty arrowheads) in outer molecular layers for DS_L and middle

molecular layers for DS_M. The CSD of the evoked response to medial perforant path (MPP) stimulation (right), evokes sinks (white empty arrowheads) at the same locations of the DS_M sinks. A ~6 ms latency sink at CA1 *stratum radiatum* occurs after both the MPP evoked response and DS_M (white full arrowheads), but not DS_L. C) Average LFP of DS_L (yellow) and DS_M (blue) with width and amplitude comparisons (bottom). D) Histograms illustrate that DS_M often follows DS_L (top) and the probability of observing $DS_L \rightarrow DS_M$ vs. $DS_M \rightarrow DS_L$ pairs (bottom). E) Average CSDs of DS_L (top) and DS_M (bottom) during stillness (speed < 2 cm/s; left) and running (speed > 3 cm/s; right). F) Relationship between DS rates and the mouse's speed. Averages ± S.E.M. are plotted.

DS_M events often follow DS_L events

Comparing the morphology of DS_L and DS_M events (Fig. 2C), DS_M width is greater than DS_L (paired $t_8 = 8.56$, $p = 10^{-5}$) while DS_L amplitude is moderately larger than DS_M (paired $t_8 = 2.87$, $p = 0.02$). DS_M has a higher shoulder ~25 ms before the peak, and DS_L has a higher shoulder about ~25 ms after the peak. The probability of observing DS_L before DS_M is greater than the probability of observing DS_M before DS_L (Fig. 2D; paired $t_8 = 5.61$, $p = 10^{-4}$). The average CSDs of DS_L and DS_M during stillness (speed < 2 cm/s) and running (speed > 3 cm/s) do not visibly differ (Fig. 2E). Rates of DS_L and DS_M events are not different, but both types of DS are differentially modulated by speed. DS_M rates increase linearly with speed, whereas DS_L do not (Fig. 2F; 2-way type x speed $ANOVA_{r.m.}$, type: $F_{1,14} = 0.02$, $p = 0.88$; speed: $F_{3,12} = 5.53$, $p = 0.013$; interaction: $F_{3,12} = 5.26$, $p = 0.015$, post-hoc tests: $DS_M > DS_L$ at the greatest speeds of 6-8 cm/s). Thus DS_L and DS_M are distinct in origin and morphology but not independent, are modulated by behavior, and DS_M is more likely to follow DS_L.

Dentate spikes modulate oscillatory activity in CA1

To determine whether DS_L and DS_M influence CA1 oscillatory activity components of SG_{dom}, we first compute event-triggered wavelet spectrum averages centered at each type of dentate spike, but the wavelet spectrum was contaminated by the spectral leakage of DS events in 30-50 Hz range, preventing independent analysis of the CA1 oscillatory dynamics (Fig. 3A). Importantly, independent component analysis (ICA) identifies two CA1 independent components (ICs) below 100 Hz (Fig. 3B), a *stratum radiatum*-localized slow gamma IC (*sr* IC; mean frequency 34.1 $\pm$ 3.0 Hz; Fig. 3C, left; Fig. S3) and a *lacunosum moleculare*-localized mid-frequency gamma IC (*slm* IC; mean frequency 68.9 $\pm$ 3.4 Hz; Fig. 3C, right; Fig. S3). We next analyze the CA1 *stratum pyramidale* theta (6-12 Hz) phase distribution of the discrete oscillatory events that are identified in the two ICs. We obtain the time-frequency wavelet spectrogram, identify local peaks > 2.5 S.D. in the z-scored power (similar to Fig. 1B) within 25-45 Hz for *sr* IC and 45-85 Hz for *slm* IC, and use the peak times to extract the corresponding theta phase using Hilbert-transformed 6-12 Hz band-pass filtered *stratum pyramidale* LFPs. The *sr* IC oscillatory events occur close to the theta trough (339.2° $\pm$ 71.4°) similar to DS_M events (344.0° $\pm$ 59.8; Watson-Williams multi-sample test $F_{1,15}$ = 0.19, p = 0.67), whereas the *slm* IC oscillatory events occur close to the theta peak (220.5° $\pm$ 59.9°) similar to DS_L events (233.6° $\pm$ 71.2°; Watson-Williams multi-sample test $F_{1,15}$ = 3.48, p = 0.08; Fig. 3D). Thus, like slow and mid-frequency gamma in CA1 (Fernandez-Ruiz et al., 2017; Lasztoczi and Klausberger, 2014), DS_M and DS_L along with *sr* IC and *slm* IC oscillation power is modulated by distinct theta phases (Fig. 3D).

The theta phase alignment of DS_L and *slm* IC events and the distinct phase alignment of DS_M and *sr* IC events might be expected if DS events control CA1 gamma events, motivating us to determine whether DS events influence the locally-generated CA1 gamma power. We compute DS_L- and DS_M-triggered IC power profiles by averaging the z-scored wavelet spectrogram across 25-45 Hz for *sr* IC and 45-85 Hz for *slm* IC (Fig. 3E). To evaluate if the potential

influence of the DS events on the CA1 ICs is distinct from the theta modulation of IC power (see Fig. 3D), we also computed power profiles triggered by random events that were sampled from the DS_L and DS_M theta phase distributions. Accordingly, the random profiles that have the same theta phase distribution as the corresponding DS events, but only a chance association with the DS events are used for statistical comparisons. Data from 8 of 9 mice are analyzed because one mouse did not have CA1 electrode coverage. The *slm* IC is strongly increased at the DS_L peak compared to random (paired $t_7 = 6.82$, $p = 10^{-4}$), while the *sr* IC is not (paired $t_7 = 0.35$, $p = 0.7$; Fig. 3E, left). However, the *sr* IC is strongly (~60%) increased at the peak of DS_M compared to random (paired $t_7 = 5.0$, $p = 0.002$), while the *slm* IC is weakly (~10%) increased (paired $t_7 = 2.68$, $p = 0.03$; Fig. 3E, right).

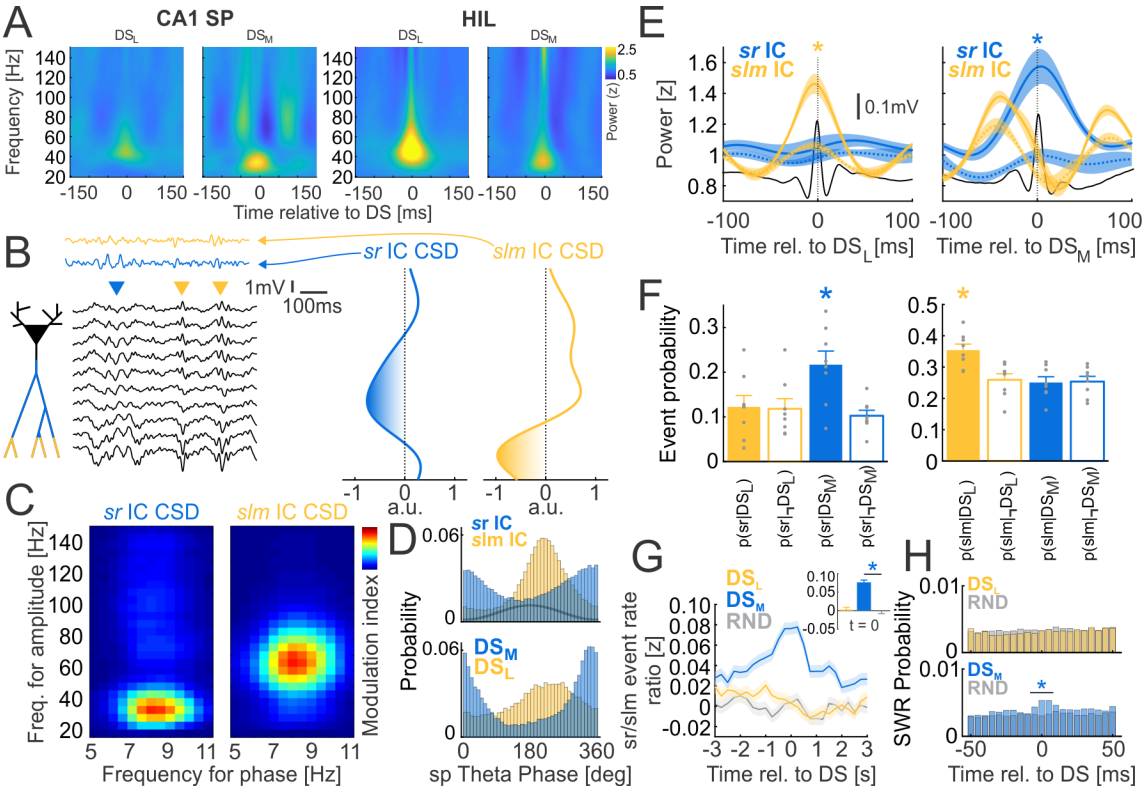

Figure 3. Dentate spikes modulate oscillatory activity in CA1, with SG_{dom} increased around DS_M A) Average wavelet spectrogram of CA1 *stratum pyramidale* LFP (CA1 SP) and dentate hilar LFP (HIL), triggered by DS_L and DS_M events reveals non-specific patterns of

activity defined by volume-conducted potentials associated with the DS spectral leakage in the 30-50 Hz range. Notice that peak frequency corresponds to different widths of DS events (compare with Fig. 2C). B) ICA decomposition of CA1 LFPs identifies two IC components < 100 Hz that correspond to *stratum radiatum* dendritic input (*sr* IC, slow gamma, blue), and *stratum lacunosum moleculare* dendritic input (*slm* IC, mid-frequency gamma, yellow). Arrowheads mark slow gamma (blue) and mid-frequency gamma (yellow) oscillatory events. The CSDs of ICA voltage loadings (right) show a *sr* IC sink in *stratum radiatum* and a *slm* IC sink in *stratum lacunosum moleculare*. C) Comodulograms between the theta (5-11 Hz) phase of CA1 hippocampal oscillations and the *sr* IC and *slm* IC gamma (20-150 Hz) amplitudes show frequency peaks in the slow gamma range for *sr* IC and mid-frequency gamma range for *slm* IC. D) Theta phase (black line) distribution of *sr* IC (blue) and *slm* IC (yellow) oscillatory events (top) compared to theta phase distribution of DS_M (blue) and DS_L (yellow) events (bottom). E) Power averages of *sr* IC (blue) and *slm* IC (yellow) centered on DS_L (left) and DS_M (right). T=0 marks the DS peak. Dotted profiles show IC power profiles at random times sampled from the same theta phase distributions as the corresponding DS_L and DS_M events. The DS_L and DS_M event averages are shown in black. F) Coincidence of the DS and IC oscillatory events detected from *sr* IC (left) and *slm* IC (right) at random times. G) SG_{dom} measured as the z-score normalized ratio of rates of slow gamma in the *sr* IC and mid-frequency gamma oscillatory events in the *slm* IC relative to the timing of DS_L (yellow), DS_M (blue) and random times (RND, grey). Inset for t = 0 (at DS/RND event). H) SWR probability distribution relative to the timing of DS_L (top) and DS_M (bottom) and random times (gray) during stillness. Averages ± S.E.M. are plotted.

To examine the co-occurrence of the DS and the CA1 gamma oscillatory events, we pick 1000 random times from each 30-min recording and assess whether an oscillatory event in the CA1 *sr* IC or *slm* IC occurs within a 50-ms coincidence interval of DS_L or DS_M. The probability of

observing an *sr* IC oscillation is greater if a DS_M is observed [Fig. 3F, left; ANOVA $F_{3,31} = 9.59$, $p = 10^{-4}$, $p(sr \mid DS_M) > p(sr \mid DS_L) = p(sr \mid \neg DS_M) = p(sr \mid \neg DS_L)$] while the probability of observing a *slm* IC oscillation is greater if a DS_L event is observed [Fig. 3F, right; ANOVA $F_{3,31} = 7.31$, $p = 10^{-4}$, $p(slm \mid DS_L) > p(slm \mid DS_M) = p(slm \mid \neg DS_L) = p(slm \mid \neg DS_M)$].

Within the hypothesis that DS events control CA1 information processing mode, these findings of DS modulation of CA1 gamma predict that DS_M (but not DS_L) promotes SG_{dom} in CA1. We assess the prediction by computing the ratio of oscillatory event rates detected in *sr* and *slm* ICs within 3 s of DS_L, DS_M, and random events (Fig. 3G). Indeed, the CA1-localized SG/MG ratio is maximal at the time of DS_M but not different from chance during DS_L (ANOVA $F_{2,70146} = 62.38$, $p < 10^{-16}$; $DS_M > DS_L = RND$). Then, because of the previously reported relationships between DS and sharp-wave ripple (SWR) events (Bragin et al., 1995), we compute the probability of a SWR within ±50 ms of DS_L, DS_M, and random events during stillness (speed < 2 cm/s). This shows a selectively increased SWR probability in the vicinity of the DS_M peak (Fig. 3H; One sample test for proportions in 20 ms window centered on DS/RND events; $p(SWR, DS_L) = 0.012$, $z = -0.71$, $p = 0.3$; $p(SWR, DS_M) = 0.018$, $z = 13.20$, $p = 10^{-39}$). These findings identify that DS_M but not DS_L in dentate gyrus modulates CA3-originating, *stratum radiatum*-localized CA1 slow gamma band oscillatory activity, the occurrence of CA3-originating ripple events, and promotes SG_{dom} in CA1.

Dentate spikes modulate CA1 gamma oscillations with ~10 millisecond precision, DS_M promoting SG_{dom}

If DS_M events control CA1 information processing by promoting SG_{dom}, then DS_M should influence CA1 gamma oscillations with a precision comparable to the ~7 ms conduction time from dentate gyrus to CA1 (Fig. 2B, solid arrowheads). Because oscillatory power can only be studied at relatively long timescales comparable to theta cycles ~100 ms (e.g. Fig. 3E), we

developed a method to analyze individual cycles of oscillatory events identified in ICs (see Materials and Methods). The local minima (red arrowheads in Fig. 4A inset) are selected because spiking and therefore information transfer is maximal (Dvorak and Fenton, 2014; Lasztoczi and Klausberger, 2016; Schomburg et al., 2012)(Fig. S4). This improves the analysis time resolution to 17 ms; half the period of the slowest *sr* IC (34 Hz). The probability of observing *slm* IC cycle minima is strongly enhanced during the peak of DS_L (20-ms window centered on DS_L versus chance: paired $t_7 = 5.43$, $p = 0.001$; Fig 4A, left) as well as 15 ms before and 16 ms after the DS_L peak, corresponding to an *slm* IC oscillatory frequency of 69 Hz, while the probability of observing *sr* IC cycle minima remains unchanged during DS_L (20-ms window centered on DS_L versus chance: paired $t_7 = 0.69$, $p = 0.52$; Fig 4A, left). In contrast, the probability of observing *sr* IC cycle minima is enhanced 6 ms after the peak of DS_M, corresponding to the transmission delay between DG and CA1, which is primarily influenced by CA3-CA1 synaptic delay (Mizuseki et al., 2012; 20-ms window centered on DSM versus chance: paired t7 = 4.52, p = 0.003; Fig 4A, right) as well as 24 ms before and 33 ms after the DS_M peak corresponding to a *sr* IC oscillatory frequency of 34 Hz, while the probability of observing *slm* IC cycle minima is not different (20-ms window centered on DS_M versus chance: paired $t_7 = 0.79$, $p = 0.45$; Fig 4A, right). There is a non-oscillatory increase of the *slm* IC cycle minima probability before DS_M (50-30 ms before DS_M versus chance: paired $t_7 = 3.80$, $p = 0.007$; Fig 4A, right) and a strong reduction of the probability of observing *slm* IC cycle minima after DS_M (30-50 ms after DS_M versus chance: paired $t_7 = 7.39$, $p = 10^{-4}$; Fig 4A, right).

This last observation raises the intriguing possibility that DS_M both increases the likelihood of CA1 slow gamma oscillations and attenuates the likelihood of CA1 mid-frequency gamma oscillations, promoting SG_{dom}. Because *slm* inputs contribute CA1 mid-frequency gamma oscillations (Figs. 3E, F) one mechanism for the DS_M-initiated *slm* IC attenuation could be that DS_M also activates preferential inhibition of the distal CA1 dendrites in *stratum lacunosum*

moleculare. We assess this possibility by examining the CSD source that might be a result of increased inhibitory drive that is strongest ~10ms after DS_M (red rectangle in Fig. 4B, left). This corresponds to the DG→CA1 transmission delay and localizes to the vicinity of the hippocampal fissure extending to CA1 *slm*, as well as the adjacent outer molecular layer in the supraDG, but is also observed at the infraDG outer molecular layer (red arrow in Fig 4B, left). To test whether this dorsal DS_M-initiated current source is associated with modulation of oscillatory cycle minima, we sort the DS_M events by the strength of the average current within the supraDG region of interest (red rectangle in Fig. 4B, left) that covers both *slm* and the outer molecular layer of DG (Fig. 4B, middle). We then compute the average DS_M CSDs for the strongest and weakest 10% of the DS_M-associated current sources (Fig. 4B, right) and estimate the probability distributions of the *sr* and *slm* oscillatory cycle minima around the two classes of DS_M events. Both the strong and weak DS_M events differentially modulate oscillatory cycle minima (2-way DS_M class x IC ANOVA in 20-ms windows centered on DS_M: DS_M class: $F_{1,47} = 13.75$, $p = 10^{-4}$; IC: $F_{1,47} = 9.74$, $p = 0.003$; Interaction: $F_{2,47} = 18.77$, $p = 10^{-6}$). *The slm* IC cycle minima are strongly attenuated during DS_M events associated with the strongest current source compared to DS_M events associated with the weakest current source (Fig. 4C, top; inset 2-4; 20-ms window centered on DS_M: paired $t_7 = 6.32$, $p = 0.0004$). In contrast, *sr* IC cycle minima are strongly increased during DS_M events associated with the strongest current source compared to DS_M events associated with the weakest current source (Fig. 4C, top; inset 2-4; 20-ms window centered on DS_M: paired $t_7 = 4.05$, $p = 0.005$). Additionally, DS_M events associated with the strongest current source show increased slm IC cycle minima before DS_M (Fig. 4C, top left; inset 1; 50-30 ms before DS peak: paired $t_7 = 6.63$, $p = 0.0003$), but attenuated *slm* IC cycle minima after DS_M when compared to random times (Fig. 4C top, left; inset 3; 30-50 ms after DS_M peak: paired $t_7 = 2.65$, $p = 0.03$). These findings indicate that DS_M events can both increase CA1 *sr* IC slow gamma oscillations and attenuate CA1 *slm* IC mid-frequency gamma oscillations, thereby promoting SG_{dom} (Fig. 4D).

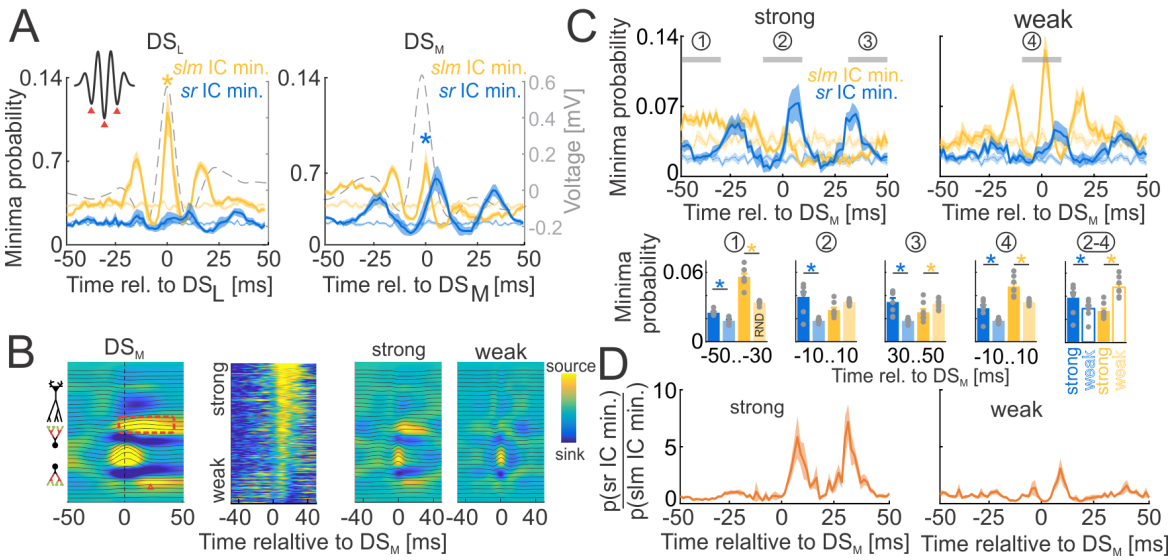

Figure 4. DS$_M$ promotes SG dominance. A) Probability of oscillatory cycle minima (inset) detected in *sr* ICs and *slm* ICs around the times of DS$_L$ (left) and DS$_M$ (right). DS averages shown as dashed lines for reference. B) A CSD source follows DS$_M$ (red rectangle and arrowhead), which can be due to DS$_M$-related inhibition at slm, as well as the outer molecular layers of supraDG and infraDG. DS$_M$ events sorted by the amplitude of the CSD source that follows DS$_M$ (middle). CSD averages of DS$_M$ events with the 10% strongest and 10% weakest CSD supraDG sources (right). C) Probability of oscillatory cycle minima in *sr* IC (blue) and *slm* IC (yellow) events around DS$_M$ with the strongest (left) and weakest (right) CSD sinks. Average probability of minima during 50-30 ms before (inset 1), 20 ms centered at (insets 2, 4 and 2-4) and 30-50 ms after (inset 3) DS$_M$ events. D) Ratio of probabilities of SG-associated oscillatory cycle minima in sr IC and MG-associated oscillatory cycle minima in slm IC during DS$_M$ with the strongest (left) and weakest (right) CSD sinks. Averages ± S.E.M. are plotted.

DS$_M$ synchronizes DG and CA1 slow gamma band oscillations

The slow gamma associated *sr* dendritic input to CA1 that increases during DS$_M$ originates in CA3; could CA3 be under enhanced or reduced DG influence during DS$_M$ (Flynn et al., 2015)?

We studied synchrony of CA1 and DG oscillations during DS_L and DS_M, starting with ICA component identification of DG LFPs, as was done with CA1 LFPs. ICA analysis combined with CSD-based classification of DS events effectively disentangles DS events and DG oscillatory components, even though they share an origin in the perforant path projection to DG (Fig. S4). Two DG components below 100 Hz are also identified (Barth et al., 2018; Fernandez-Ruiz et al., 2013). The lateral perforant path (LPP) IC is associated with outer molecular layer DG sinks in the CSD of the ICA voltage loadings and a slow gamma peak in the comodulogram with CA1 theta phase (mean frequency 43.9 $\pm$ 5.0 Hz). The medial perforant path (MPP) IC is associated with middle molecular layer DG sinks in the CSD of the ICA voltage loadings and a mid-frequency gamma peak in the comodulogram with CA1 theta phase (mean frequency 71.0 $\pm$ 2.7 Hz). While the mean frequency of the LPP IC component is higher than the mean frequency of CA1 *sr* IC (paired $t_6 = 3.69$, $p = 0.01$), the mean frequency of the MPP IC does not differ from the mean frequency of the CA1 slm IC (paired $t_6 = 2.17$, $p = 0.07$). Next, we use CA1 theta as an intrinsic network time reference, and analyze the CA1 theta phase preference of the dentate ICs (Fig. 5A). The slow gamma LPP IC occurs at a late descending phase, close to the theta trough (277.4° $\pm$ 74.3°) that precedes both DS_M (Watson-Williams multi-sample test $F_{1,14} = 6.3$, $p = 0.03$) and slow gamma *sr* IC (Watson-Williams multi-sample test $F_{1,14} = 4.5$, $p = 0.05$). The mid-frequency gamma MPP IC occurs close to the theta peak (214.9° $\pm$ 59.8°), similar to DS_L (Watson-Williams multi-sample test $F_{1,14} = 1.9$, $p = 0.19$) as well as mid-frequency gamma *slm* IC (Watson-Williams multi-sample test $F_{1,14} = 0.04$, $p = 0.83$).

To study the phase coupling between the DG and CA1 slow and mid-frequency gamma IC components, we compute peri-DS phase locking values (PLV) between components in a wide 20-100 Hz frequency range (Fig. 5B, C). Fig. 5B shows that the DG slow gamma LPP IC and the CA1 slow gamma *sr* IC are not coupled during DS_L (Fig. 5B, top left), whereas the mid-frequency gamma MPP IC and the CA1 mid-frequency gamma *slm* IC couple during DS_L (Fig.

5B, bottom left). In contrast, the DG and CA1 slow gamma LPP IC and *sr* IC couple slightly after DS_M (Fig. 5B, top right), and the mid-frequency gamma MPP and *slm* ICs also couple ~50 ms before and ~75 ms after DS_M (Fig. 5B, bottom right). Although the PLV is computed in a wide frequency range 20-100 Hz, the phase interactions occur in relatively narrow bands, especially in the case of the DS_M-timed events, pointing to the frequency specificity of the coupled IC components. To evaluate whether these effects are in excess of expectations given the theta phase modulation of these IC components (see Figs. 3D, 5A), we also compute the PLV around randomly selected time points that are sampled from the theta phase distributions of the DS_L and DS_M events (gray profiles in Fig. 5C). We average the PLV values across the frequency bands of interest (25-45 Hz) for slow gamma ICs and 45-85 Hz for mid-frequency gamma ICs. The only significant departure from random phase locking during DS_M is between the dentate LPP IC and the CA1 *sr* IC in the slow gamma range (Fig. 5C, top right; paired $t_6 = 4.04$, $p = 0.006$). The peak of this phase locking occurs 9 ms after the DS_M peak. Furthermore, DS_M-locked CA1 *sr* IC oscillatory cycle minima (Fig. 4A) lag DG LPP oscillatory cycle minima by 6 ms (Fig. S5) pointing again to the same DG→CA1 transmission delay that was observed in Figs. 2B and 4A.

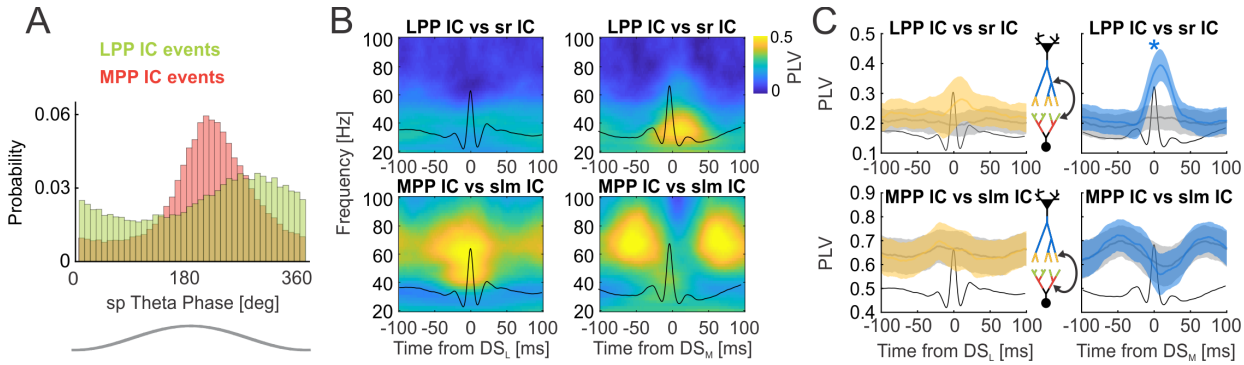

Figure 5. DS_M synchronizes slow gamma LPP oscillatory inputs to dentate gyrus and CA3 inputs to CA1 *stratum radiatum*. A) Theta phase distribution of oscillatory events in the LPP IC (green) and the MPP IC (red). B) Example of wide-band phase locking (PLV) between the

slow gamma LPP and the *sr* ICs (top) and between the mid-frequency gamma MPP and *slm* ICs (bottom) time-locked to DS_L (left) and DS_M (right). Average DS_L and DS_M are in black for reference. C) Group PLV measures averaged across the slow gamma (25-45 Hz for LPP and *sr* ICs) and mid-frequency gamma bands (45-85 Hz for MPP and *slm* ICs). Gray lines are random PLV profiles sampled from the corresponding DS_L and DS_M theta phase distributions. Average DS_L and DS_M waveforms are in black. Averages ± S.E.M. are plotted.

CA1 and DG slow gamma oscillations are frequency- and phase-tuned during DS_M

Given a fixed duration of the gamma-generating $GABA_A$ receptor response, the frequency of a gamma oscillation can be set by adjusting the level of network excitation, with greater excitation producing faster oscillations because GABA inhibition can be overcome sooner (Whittington et al., 1995). Because slow gamma in DG (LPP IC; 44 Hz) and CA1 (*sr* IC; 34 Hz) oscillate at different frequencies, but phase lock during DS_M (Fig. 5C), the gamma-generating mechanism predicts input-driven changes in both the frequency and phase relationships for the phase alignment during DS_M. Accordingly, we analyze the frequency and phase relationships of *sr* and LPP ICs during DS_M. The time-frequency wavelet spectrum average is computed time-locked to DS_M (Fig. 6A). Then, for each timepoint ±40 ms around DS_M we find the frequency at which the maximum power occurs (black dots in Fig. 6A). During DS_M, the frequency of the LPP IC decreases from 43 Hz to 36 Hz at the peak of DS_M, whereas the frequency of *sr* IC increases from 28 Hz to 36 Hz at the peak of DS_M, effectively aligning the frequencies of the DG and CA1 originating oscillations, consistent with reduced LPP input and increased CA3 input via the Schaffer collaterals. A single-subject example of the distribution of phase differences between the LPP IC and the *sr* IC shows a mean phase difference of 111° with the LPP IC preceding the *sr* IC by about $^1/_3$ of a *sr* IC cycle corresponding to 10 ms (Fig. 6B). Because the mean phase difference varies slightly in each animal, we measure the mean phase offset between the LPP

IC and the *sr* IC for each animal independently, and then compute the deviation from the mean offset relative to DS_M for group statistics across animals (Fig. 6C). The maximum deviation differs from zero (DS_M-25 ms: t_6= 4.51, p = 0.004), and was 25 ms before the DS_M peak at the locally maximal positivity of the DS_M; the phase offset reverts to the mean by 60 ms after DS_M (versus 0 at DS_M+60 ms: t_6= 2.37, p = 0.06). At the peak of DS_M, the phase difference is reduced by 14.5±12.8° (corresponding to ~2 ms earlier), towards a more favorable difference for signal transmission, similar to the DG-CA1 transmission delay observed in (Figs. 2B, 4A, 5C and S5).

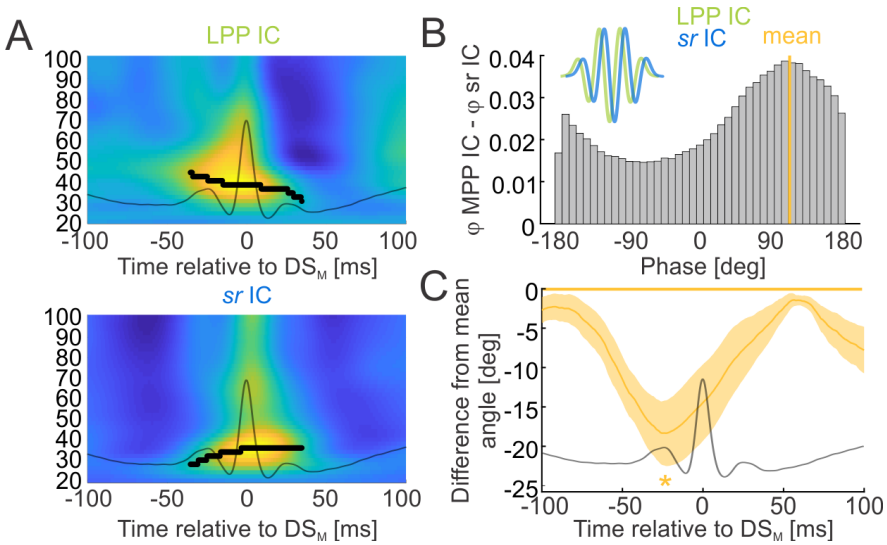

Figure 6. Frequency- and phase-tuning of slow gamma oscillations at the dentate LPP termination and the CA3 Schaffer collateral termination in CA1 *stratum radiatum* during DS_M A) Average wavelet spectrogram of the LPP IC (top) and *sr* IC (bottom) around the time of DS_M (T=0 ms). Black dots indicate frequency of peak power at each time point ±40 ms. B) Single-subject example histogram of phase differences between LPP IC and *sr* IC with mean angle identified. C) Group average of divergence of phase difference from the mean phase

difference between LPP IC and *sr* IC. Average DS_M waveform is plotted in black for reference. Averages ± S.E.M. are plotted.

DS_M increases DG, CA3 and CA1 discharge rates and cofiring

The findings together identify that DS_M events promote SG_{dom} (Figs. 3, 4), and synchronize oscillations activated at the LPP terminals in DG and *sr* of CA1 (Figs. 5, 6), presumably by facilitating DG→CA1 neural transmission. The hypothesis that DS_M has a causal role in these events predicts that DS_M coactivates DG, CA3, and CA1 discharge. Objectively classified, presumptive principal cells (PC) and narrow waveform interneurons (INTn) were localized and studied (Fig. 7A, B).

The firing rates of presumptive granule cells (GC, n = 141), mossy cells (MC, n = 140), CA3 (n = 104) and CA1 (n = 145) principal cells as well as narrow-waveform interneurons detected in their proximity (n = 435) during the 10 ms around DS_L and DS_M events (Fig. 7C) were compared with the firing rates at random times. The discharge of GC, CA3 and CA1 principal cells do not change during DS_L (Fig. 7C; GC: $t_{140} = 1.77$, $p = 0.08$; CA3: $t_{103} = 0.14$, $p = 0.88$; CA1: $t_{144} = 1.28$, $p = 0.20$) while the discharge of MC decreases by 25% (Fig. 7C; $t_{139} = 5.92$, $p = 10^{-8}$). In contrast, during DS_M, GC rates increase to 303%, MC rates increase to 217%, CA3 rates increase to 175% and CA1 rates increase to 125% of the baseline rate (Fig. 7C; GC: $t_{140} = 7.10$, $p = 10^{-11}$; MC: $t_{139} = 7.30$, $p = 10^{-11}$; CA3: $t_{103} = 4.07$, $p = 10^{-5}$; CA1: $t_{144} = 4.46$, $p = 10^{-5}$). The discharge of GC-associated (n = 96) and MC-associated (n = 89) narrow-waveform interneurons reduces by 12% and 14%, respectively, during DS_L (Fig. 7C; GC INTn: $t_{95} = 3.03$, $p = 10^{-3}$; MC INTn: $t_{88} = 3.51$, $p = 10^{-4}$) while discharge of CA3-associated (n = 102) and CA1-

associated (n = 148) narrow-waveform interneurons increases by 18% and 14%, respectively (Fig. 7C; CA3 INTn: $t_{101} = 4.10$, $p = 10^{-5}$; CA1 INTn: $t_{147} = 4.05$, $p = 10^{-5}$). In contrast, during DS_M, rates of GC-, MC-, CA3- and CA1-associated interneurons increase to 425%, 295%, 190% and 142% respectively (Fig. 7C; GC INTn: $t_{95} = 13.05$, $p = 10^{-23}$; MC INTn: $t_{88} = 8.93$, $p = 10^{-14}$; CA3 INTn: $t_{101} = 7.46$, $p = 10^{-11}$; CA1 INTn: $t_{147} = 8.14$, $p = 10^{-13}$).

These findings suggest that DS_L events result in net inactivation of both excitatory and inhibitory cells in DG and weak activation of interneurons in CA3 and CA1, without changing the firing rates of CA3 and CA1 principal cells, whereas DS_M events result in strong activation of both excitatory and inhibitory cells along the DG→CA3 →CA1 trisynaptic pathway. The DS_M-associated increase of both excitatory and inhibitory cells establishes the neurophysiological conditions for enhanced temporal control of principal cell discharge through the mechanisms of excitation-inhibition coupling, and enhanced opportunities for cofiring that can enhance neural transmission across the entire DG→CA3 →CA1 trisynaptic pathway (Renart et al., 2010).

Accordingly, we analyze the cofiring of pairs of cells during DS_L, DS_M and random events by computing a peri-DS-event cofiring probability histogram for each cell pair (Fig. 7D). Because the highest probability of observing coactive cell pairs typically occurs at the peak of DS_M events (Fig. 7D, bottom), we quantify each cofiring relationship by comparing the cofiring probability in a 6 ms window centered at the DS event to the cofiring probability at random times. Each cofiring relationship is statistically evaluated using a t test between cofiring probabilities normalized by marginal probabilities of discharge of each cell, to account for the general increase of firing during DS events; significance is adjusted using Bonferroni's method.

The firing rate increases during DS_M predict increased excitatory-inhibitory co-firing during DS_M to promote SG_{dom} in CA1, as does a recent finding that the cofiring between pairs of excitatory and inhibitory cells increases in dentate gyrus during moments of active and successful memory discrimination (van Dijk and Fenton, 2018). Accordingly, we compare cofiring between

presumptive excitatory (PCs) and inhibitory (INTn) cells within each of the GC, MC, CA3 and CA1 regions (Table S1). During DS_M, cofiring amongst the GC and associated interneuron populations increases relative to random times (Fig. 7D, left; 684±788 %, $t_{528} = 3.49$, $p = 10^{-3}$), whereas the cofiring decreases during DS_L (65±97 %, $t_{528} = 3.65$, $p = 10^{-4}$). PC and INTn cofiring within CA3 also increases during DS_M (254±329 %, $t_{489} = 4.11$, $p = 10^{-5}$) but does not change during DS_L (106±131 %, $t_{489} = 2.71$, $p = 0.007$). No changes in co-firing between PC and INTn are observed within CA1. Discharge coupling between PC and INTn cells selectively increases in CA3 during DS_M compared to DS_L ($t_{564} = 3.07$, $p = 10^{-3}$) indicating potentially increased inhibitory control of principal cell spiking during the DS_M events. Consistent with this finding, we also observe strongly increased cofiring during DS_M but not DS_L between MC- and GC-associated interneurons (648±648 %, $t_{123} = 4.64$, $p = 10^{-6}$) and also DS_M-related cofiring between GC and CA3 principal cells (140±111 %, $t_{67} = 3.19$, $p = 10^{-3}$) and CA3 interneurons (253±328 %, $t_{489} = 4.11$, $p = 10^{-5}$). Taken together, DS_M events selectively activate local inhibitory networks in both DG and CA3, which control neuron cofiring between the GC and CA3 networks, perhaps to promote SG_{dom} in CA1 (Fig. 7D, right).

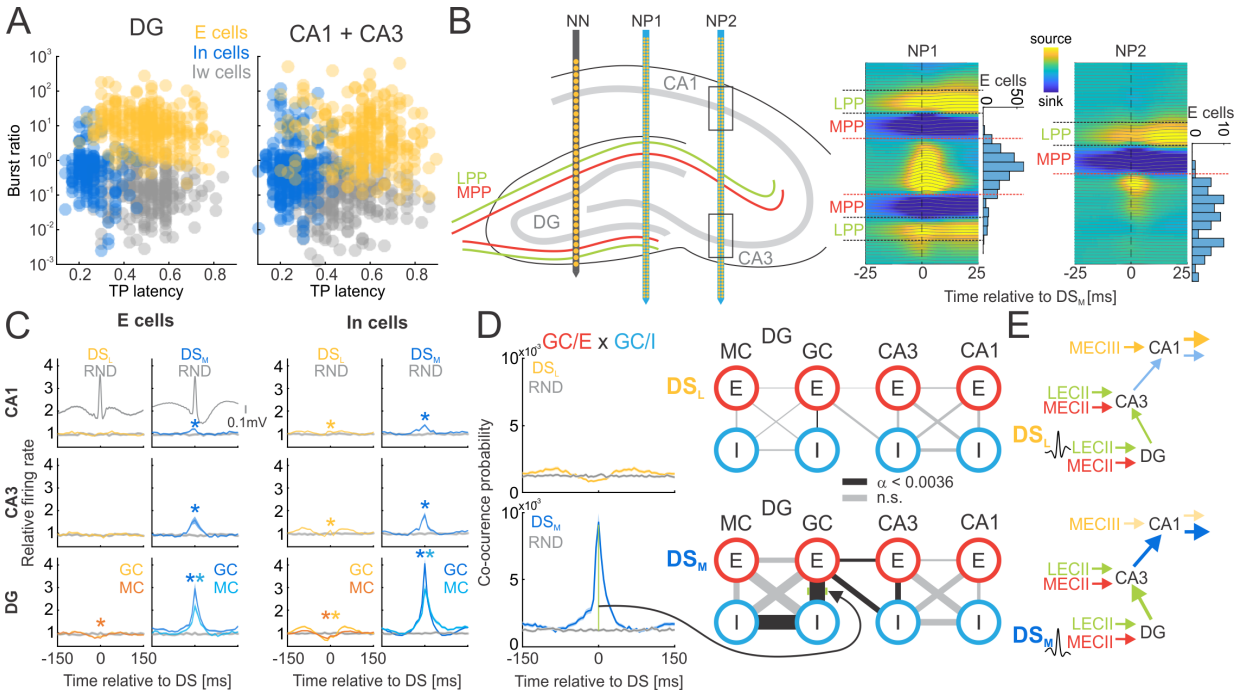

Figure 7. DS_M increases DG, CA3, CA1 firing and DG-CA3 cofiring. A) Unitary action potentials were classified as being from excitatory cells (E), narrow-waveform interneurons (In) and wide-waveform interneurons (Iw) using the K-means algorithm on the DG-localized (left) and separately, the CA3- and CA1-localized datasets (right). B) Schematic mouse hippocampus (left) with medial placement of Neuronexus linear electrode array (NN) for detection of DS events and two example lateral placements of Neuropixel probes. NP1 represents location proximal to DG, NP2 represents location proximal to CA3. The connection asymmetry of the lateral and medial perforant paths (LPP and MPP) distinguishes DG and CA3 localization. Rectangles along NP2 show regions of CA1 and CA3 samples. DS_M-triggered CSD of LFP at location NP1 (middle) shows symmetrical MPP sinks, while the NP2 location (right) shows an asymmetrical MPP sink present only at the dorsal molecular layer of DG. Depth distributions of putative excitatory cells from NP1 and NP2 locations are shown on the right side of CSDs. Red dotted lines represent granule cell layer, black dotted lines represent borders of outer molecular layers of DG. C) Normalized firing rates of CA1 (top), CA3 (middle), and DG (bottom) during DS_L (left) and DS_M (right) and random (gray) events. DS averages shown as dashed lines for reference. D) Cofiring probability of pairs of GC principal cells (GC/E) and proximal narrow waveform interneurons (GC/I) in a 6 ms window around DS_L (left, top, yellow) and DS_M (left, bottom, blue) and random (gray) events. Ratio between cofiring probability during DS events and random times is represented as line thickness (right) in a DG-CA3-CA1 network schematic; the black connections significantly differ from random times, while grey connections do not. Significance adjusted using Bonferroni's method (Table S1). E) Proposed mechanism of extrahippocampal control of hippocampus function. Averages ± S.E.M. are plotted.

Having identified a mechanism by which DS_M promotes SG_{dom} and increased CA1 discharge we examined the unintuitive prediction that during free exploration, place cells will discharge

less than expected when mice walk across a cell's place field during SG_{dom}. This is because the increased discharge will preferentially represent non-local positions that do not correspond to the cell's firing field. Indeed, the standardized rate (z) of place cells during passes through the firing field is lower during SG_{dom}, than during MG_{dom}, and RND events (Fig. S7C; $F_{2,521} = 3.16$, $p = 0.04$, $SG_{dom} < MG_{dom} = RND$) while the overdispersion of place cell discharge was similar across the three conditions (Fig. S7B; SG_{dom}: var = 4.25; MG_{dom}: var = 4.80; RND: var = 5.11; $F_{2,521} = 1.03$, $p = 0.4$), comparable to published values for mice and rats (Fenton et al., 2010; Fenton and Muller, 1998; Jackson and Redish, 2007; Talbot et al., 2018b). These findings add to the evidence that during SG_{dom}, CA1 discharge is distinct, and poorly predicted by current physical variables; this distinctive mode of hippocampus information processing is controlled by DS_M.

Discussion

Conclusion

We identify DS_M dentate spikes as a mechanism that can promote SG_{dom} events in CA1 that switch hippocampus from encoding currently experienced information to recollecting information from the past. This is observed for example, as CA1 place cell discharge signaling the current location switching to the SG_{dom}-associated non-local CA1 discharge that signals recollected locations of shock a mouse actively avoids (Dvorak et al., 2018). DS_M at the termination zone of the medial perforant path in the dentate gyrus, control the likelihood of SG_{dom} events in CA1, and induce changes throughout Ammon's horn, consistent with the notion that they trigger a transient change in overall hippocampus function. In contrast, the consequences of DS_L events in Ammon's horn were mostly indistinguishable from baseline activity.

DS_M control of information processing in Ammon's horn

Our findings demonstrate extrahippocampal cortical control of information processing in hippocampus mediated by DS_M, the result of the synchronous activation of medial perforant path terminals at the middle molecular layer of dentate gyrus (Fig. 2; Bragin et al., 1995). The effects of DS_M are in dramatic and consistent contrast to the effects of DS_L, making it essential to distinguish them. In fact, conclusions based on work that did not discriminate DS_L from DS_M, have been misleading. Whether DS events activate or suppress dentate gyrus output to CA3 was uncertain. DS events were reported to couple to synchronous population bursts of putative hilar inhibitory interneurons and reduce multiunit CA3 and CA1 spiking (Bragin et al., 1995), suggesting that DS suppresses dentate output. This suppression was not subsequently confirmed (Flynn et al., 2015), but the idea that DS events are anti-excitatory was supported by increased DS prevalence in compensation for increased entorhinal excitation in pilocarpine-induced status epilepticus (Flynn et al., 2015). We observe that DS_L is associated with decreased discharge of DG principal cells (Fig. 7). In stark contrast, DS_M massively increased discharge of presumptive dentate principal cells and interneurons as well as CA3 principal cells, demonstrating that DS_M (but not DS_L) events result in strong dentate and CA3 activation through the EC→DG→CA3 circuit (Fig. 7). While this does not support the anti-excitatory notion, suggested by prior work that did not distinguish DS_L and DS_M, our findings are consistent with the reduced population spike latency, increased population spike amplitude, and enhanced field excitatory postsynaptic potential (fEPSP) slope that were observed during medial perforant path (MPP) stimulation triggered by undifferentiated DS events (Bramham, 1998). Indeed, we have observed that training in a place avoidance task causes synaptic plasticity of the MPP synaptic response in the supraDG, and potentiation of DS_M but not DS_L, corroborating the two pathways are distinctive and can be altered independently by experience (Chung et al., preprint).

The present findings point to a process of dynamic control of hippocampal information processing marked by transient physiological events across the trisynaptic pathway. During

$SG_{dom,}$ DG, CA3, and CA1 discharge is transiently elevated along with DG-CA3 cofiring (Fig. 7), and there is slow gamma frequency and phase synchronization between LPP inputs to DG and the *stratum radiatum* input to CA1 from CA3 (Figs. 5, 6), indicating involvement of the entire trisynaptic pathway, like during SWR (Buzsaki et al., 2003; Sullivan et al., 2011). Indeed, during DS_M, SWR probability in a 20 ms window increases from 1.2% to 1.8% (Fig. 3H) and place cell discharge is non-local during SWR (Buzsaki, 2015; O'Neill et al., 2006; Papale et al., 2016; Sullivan et al., 2011) as well as during SG_{dom} (Fig. S7; Dvorak et al., 2018).

The qualitative distinction between information signaled by LEC and MEC is important in this context. LEC transmits contextual information based on objects and egocentric information that constitutes the content of spatial experience (Knierim et al., 2014; Tsao et al., 2013; Wang et al., 2018), whereas MEC transmits allocentric spatial signals like direction, distance, borders, and speed (Rowland et al., 2018; Sargolini et al., 2006; Ye et al., 2018). Remarkably, the MEC-originating DS_M signal that promotes SG_{dom} and switches CA1 to non-local positional memory processing is coincident with synchronization between CA3-transmitted slow gamma inputs to CA1 and LEC-transmitted slow gamma inputs to DG, rather than from MEC (Fig. 5). Within the "communication through coherence" hypothesis (Fries et al., 2007), the LEC→DG and CA3→CA1 inputs have a privileged opportunity for information transfer via synchronized slow gamma transmission, and so we speculate that perhaps while switching the hippocampal information processing mode, DS_M loads Ammon's horn with information from the LEC-delivered egocentric contents of experience. In this way, during DS_M, the consequent activation of CA3 may be preferentially influenced by contextual and egocentric, ecphoric retrieval cues delivered by the LEC inputs (Kelemen and Fenton, 2013; Tulving et al., 1983). If these manifest as SG_{dom} because of the strong DS_M-associated activation of CA3 (Fig. 7C), the result is control of CA1 output that overrides the default control that is exerted by the mid-frequency gamma mediated ECIII input at *slm* (Brun et al., 2002). These *slm* inputs appear necessary for place cell

firing (Brun et al., 2008), and they create permissive dendritic depolarization (Jarsky et al., 2005), but in principle can be shunted by the slow gamma-associated inputs (Keeley et al., 2017), and are possibly actively inhibited as a consequence of DS_M (Fig. 4C), all of which promote SG_{dom} (Fig. 3G). As we have observed during SG_{dom}, CA1 discharge will signal non-local positions that during a memory task, correspond to recollected places (Dvorak et al., 2018), and we observed here a correspondingly reduced local discharge by place cells in their firing fields (Fig. S7), despite overall increased CA1 firing (Fig. 7C). Indeed, the findings of a hippocampus-wide (Fig. 7), DS_M-promoted SG_{dom} control of hippocampus information processing to a non-local mode of information processing identify a source of the overdispersion that is characteristic of place cells in CA1, CA3, and DG (Fenton et al., 2010; Fenton and Muller, 1998; Hok et al., 2012; Jackson and Redish, 2007; van Dijk and Fenton, 2018), and also grid cells, although we cannot conclude the mechanism is the same (Nagele et al., 2020). The findings also offer an explanation for the possible utility of CA1 receiving two spatial inputs; the Schaffer collaterals provide place cell inputs that can be non-local and related to mental experience, whereas the temporoammonic pathway provides an input comprised of components of place (grid cell distances, directional cells, border cells, and speed cells) more tethered to local, physical experience.

References

Barth, A.M., Domonkos, A., Fernandez-Ruiz, A., Freund, T.F., and Varga, V. (2018). Hippocampal Network Dynamics during Rearing Episodes. Cell Rep 23, 1706-1715.

Bragin, A., Jando, G., Nadasdy, Z., van Landeghem, M., and Buzsaki, G. (1995). Dentate EEG spikes and associated interneuronal population bursts in the hippocampal hilar region of the rat. J Neurophysiol 73, 1691-1705.

Bramham, C.R. (1998). Phasic boosting of medial perforant path-evoked granule cell output time-locked to spontaneous dentate EEG spikes in awake rats. J Neurophysiol 79, 2825-2832.

Brun, V.H., Leutgeb, S., Wu, H.Q., Schwarcz, R., Witter, M.P., Moser, E.I., and Moser, M.B. (2008). Impaired Spatial Representation in CA1 after Lesion of Direct Input from Entorhinal Cortex. Neuron 57, 290-302.

Brun, V.H., Otnass, M.K., Molden, S., Steffenach, H.A., Witter, M.P., Moser, M.B., and Moser, E.I. (2002). Place cells and place recognition maintained by direct entorhinal-hippocampal circuitry. Science 296, 2243-2246.
Buzsaki, G. (2015). Hippocampal sharp wave-ripple: A cognitive biomarker for episodic memory and planning. Hippocampus 25, 1073-1188.
Buzsaki, G., Buhl, D.L., Harris, K.D., Csicsvari, J., Czeh, B., and Morozov, A. (2003). Hippocampal network patterns of activity in the mouse. Neuroscience 116, 201-211.
Chung, A., Garcia-Jou, C., Dvorak, D., Hussain, N., and Fenton, A. (preprint). Learning to learn persistently modifies a cortical-hippocampal excitatory-inhibitory subcircuit. bioRxiv, 817627.
Colgin, L.L. (2015). Do slow and fast gamma rhythms correspond to distinct functional states in the hippocampal network? Brain Res 1621, 309-315.
Csicsvari, J., Hirase, H., Czurko, A., Mamiya, A., and Buzsaki, G. (1999). Fast network oscillations in the hippocampal CA1 region of the behaving rat. J Neurosci 19, RC20.
de Almeida, L., Idiart, M., and Lisman, J.E. (2009). A second function of gamma frequency oscillations: an E%-max winner-take-all mechanism selects which cells fire. J Neurosci 29, 7497-7503.
Dvorak, D., and Fenton, A.A. (2014). Toward a proper estimation of phase-amplitude coupling in neural oscillations. J Neurosci Methods 225, 42-56.
Dvorak, D., Radwan, B., Sparks, F.T., Talbot, Z.N., and Fenton, A.A. (2018). Control of recollection by slow gamma dominating mid-frequency gamma in hippocampus CA1. PLoS Biol 16, e2003354.
Fenton, A.A., Lytton, W.W., Barry, J.M., Lenck-Santini, P.P., Zinyuk, L.E., Kubik, S., Bures, J., Poucet, B., Muller, R.U., and Olypher, A.V. (2010). Attention-like modulation of hippocampus place cell discharge. J Neurosci 30, 4613-4625.
Fenton, A.A., and Muller, R.U. (1998). Place cell discharge is extremely variable during individual passes of the rat through the firing field. Proc Natl Acad Sci U S A 95, 3182-3187.
Fernandez-Ruiz, A., and Herreras, O. (2013). Identifying the synaptic origin of ongoing neuronal oscillations through spatial discrimination of electric fields. Frontiers in computational neuroscience 7, 5.
Fernandez-Ruiz, A., Munoz, S., Sancho, M., Makarova, J., Makarov, V.A., and Herreras, O. (2013). Cytoarchitectonic and dynamic origins of giant positive local field potentials in the dentate gyrus. J Neurosci 33, 15518-15532.
Fernandez-Ruiz, A., Oliva, A., Nagy, G.A., Maurer, A.P., Berenyi, A., and Buzsaki, G. (2017). Entorhinal-CA3 Dual-Input Control of Spike Timing in the Hippocampus by Theta-Gamma Coupling. Neuron 93, 1213-1226 e1215.
Flynn, S.P., Barriere, S., Scott, R.C., Lenck-Santini, P.P., and Holmes, G.L. (2015). Status Epilepticus Induced Spontaneous Dentate Gyrus Spikes: In Vivo Current Source Density Analysis. PLoS One 10, e0132630.
Fries, P., Nikolic, D., and Singer, W. (2007). The gamma cycle. Trends Neurosci 30, 309-316.
Hargreaves, E.L., Rao, G., Lee, I., and Knierim, J.J. (2005). Major dissociation between medial and lateral entorhinal input to dorsal hippocampus. Science 308, 1792-1794.
Harris, K.D., Csicsvari, J., Hirase, H., Dragoi, G., and Buzsaki, G. (2003). Organization of cell assemblies in the hippocampus. Nature 424, 552-556.

Headley, D.B., Kanta, V., and Pare, D. (2017). Intra- and interregional cortical interactions related to sharp-wave ripples and dentate spikes. J Neurophysiol 117, 556-565.
Hebb, D.O. (1949). The organization of behavior, a neuropsychological theory (New York: Wiley).
Hok, V., Chah, E., Reilly, R.B., and O'Mara, S.M. (2012). Hippocampal dynamics predict interindividual cognitive differences in rats. J Neurosci 32, 3540-3551.
Hyvarinen, A. (1999). Fast and robust fixed-point algorithms for independent component analysis. IEEE Trans Neural Netw 10, 626-634.
Jackson, J., and Redish, A.D. (2007). Network dynamics of hippocampal cell-assemblies resemble multiple spatial maps within single tasks. Hippocampus 17, 1209-1229.
Jarsky, T., Roxin, A., Kath, W.L., and Spruston, N. (2005). Conditional dendritic spike propagation following distal synaptic activation of hippocampal CA1 pyramidal neurons. Nat Neurosci 8, 1667-1676.
Jia, X., Siegle, J.H., Bennett, C., Gale, S.D., Denman, D.J., Koch, C., and Olsen, S.R. (2019). High-density extracellular probes reveal dendritic backpropagation and facilitate neuron classification. J Neurophysiol 121, 1831-1847.
Jun, J.J., Steinmetz, N.A., Siegle, J.H., Denman, D.J., Bauza, M., Barbarits, B., Lee, A.K., Anastassiou, C.A., Andrei, A., Aydin, C.*, et al.* (2017). Fully integrated silicon probes for high-density recording of neural activity. Nature 551, 232-236.
Keeley, S., Fenton, A.A., and Rinzel, J. (2017). Modeling fast and slow gamma oscillations with interneurons of different subtype. J Neurophysiol 117, 950-965.
Kelemen, E., and Fenton, A.A. (2010). Dynamic grouping of hippocampal neural activity during cognitive control of two spatial frames. PLoS Biol 8, e1000403.
Kelemen, E., and Fenton, A.A. (2013). Key features of human episodic recollection in the cross-episode retrieval of rat hippocampus representations of space. PLoS Biol 11, e1001607.
Kelemen, E., and Fenton, A.A. (2016). Coordinating different representations in the hippocampus. Neurobiol Learn Mem 129, 50-59.
Knierim, J.J., Neunuebel, J.P., and Deshmukh, S.S. (2014). Functional correlates of the lateral and medial entorhinal cortex: objects, path integration and local-global reference frames. Philos Trans R Soc Lond B Biol Sci 369, 20130369.
Lachaux, J.P., Rodriguez, E., Martinerie, J., and Varela, F.J. (1999). Measuring phase synchrony in brain signals. Hum Brain Mapp 8, 194-208.
Lasztoczi, B., and Klausberger, T. (2014). Layer-Specific GABAergic Control of Distinct Gamma Oscillations in the CA1 Hippocampus. Neuron 81, 1126-1139.
Lasztoczi, B., and Klausberger, T. (2016). Hippocampal Place Cells Couple to Three Different Gamma Oscillations during Place Field Traversal. Neuron 91, 34-40.
Makarov, V.A., Makarova, J., and Herreras, O. (2010). Disentanglement of local field potential sources by independent component analysis. Journal of computational neuroscience 29, 445-457.
Mizuseki, K., Royer, S., Diba, K., and Buzsaki, G. (2012). Activity dynamics and behavioral correlates of CA3 and CA1 hippocampal pyramidal neurons. Hippocampus 22, 1659-1680.
Nagele, J., Herz, A.V.M., and Stemmler, M.B. (2020). Untethered firing fields and intermittent silences: Why grid-cell discharge is so variable. Hippocampus n/a.

O'Neill, J., Senior, T., and Csicsvari, J. (2006). Place-selective firing of CA1 pyramidal cells during sharp wave/ripple network patterns in exploratory behavior. Neuron 49, 143-155.
Pachitariu, M., Steinmetz, N., Kadir, S., Carandini, M., and Harris, K.D. (2016). Kilosort: realtime spike-sorting for extracellular electrophysiology with hundreds of channels. bioRxiv 061481 (2016).
Papale, A.E., Zielinski, M.C., Frank, L.M., Jadhav, S.P., and Redish, A.D. (2016). Interplay between Hippocampal Sharp-Wave-Ripple Events and Vicarious Trial and Error Behaviors in Decision Making. Neuron 92, 975-982.
Pastalkova, E., Itskov, V., Amarasingham, A., and Buzsaki, G. (2008). Internally generated cell assembly sequences in the rat hippocampus. Science 321, 1322-1327.
Pettersen, K.H., Devor, A., Ulbert, I., Dale, A.M., and Einevoll, G.T. (2006). Current-source density estimation based on inversion of electrostatic forward solution: Effects of finite extent of neuronal activity and conductivity discontinuities. J Neurosci Meth 154, 116-133.
Renart, A., de la Rocha, J., Bartho, P., Hollender, L., Parga, N., Reyes, A., and Harris, K.D. (2010). The asynchronous state in cortical circuits. Science 327, 587-590.
Rolls, E.T., and Treves, A. (1998). Neural Networks and Brain Function (Oxford: Oxford University Press).
Rowland, D.C., Obenhaus, H.A., Skytoen, E.R., Zhang, Q., Kentros, C.G., Moser, E.I., and Moser, M.B. (2018). Functional properties of stellate cells in medial entorhinal cortex layer II. Elife 7.
Sargolini, F., Fyhn, M., Hafting, T., McNaughton, B.L., Witter, M.P., Moser, M.B., and Moser, E.I. (2006). Conjunctive representation of position, direction, and velocity in entorhinal cortex. Science 312, 758-762.
Schomburg, E.W., Anastassiou, C.A., Buzsaki, G., and Koch, C. (2012). The spiking component of oscillatory extracellular potentials in the rat hippocampus. J Neurosci 32, 11798-11811.
Schomburg, E.W., Fernandez-Ruiz, A., Mizuseki, K., Berenyi, A., Anastassiou, C.A., Koch, C., and Buzsaki, G. (2014). Theta phase segregation of input-specific gamma patterns in entorhinal-hippocampal networks. Neuron 84, 470-485.
Senzai, Y., and Buzsaki, G. (2017). Physiological Properties and Behavioral Correlates of Hippocampal Granule Cells and Mossy Cells. Neuron 93, 691-704 e695.
Sullivan, D., Csicsvari, J., Mizuseki, K., Montgomery, S., Diba, K., and Buzsaki, G. (2011). Relationships between hippocampal sharp waves, ripples, and fast gamma oscillation: influence of dentate and entorhinal cortical activity. J Neurosci 31, 8605-8616.
Talbot, Z.N., Sparks, F.T., Dvorak, D., Curran, B.M., Alarcon, J.M., and Fenton, A.A. (2018a). Normal CA1 Place Fields but Discoordinated Network Discharge in a Fmr1-Null Mouse Model of Fragile X Syndrome. Neuron.
Talbot, Z.N., Sparks, F.T., Dvorak, D., Curran, B.M., Alarcon, J.M., and Fenton, A.A. (2018b). Normal CA1 Place Fields but Discoordinated Network Discharge in a Fmr1-Null Mouse Model of Fragile X Syndrome. Neuron 97, 684-697.
Tort, A.B., Komorowski, R., Eichenbaum, H., and Kopell, N. (2010). Measuring phase-amplitude coupling between neuronal oscillations of different frequencies. J Neurophysiol 104, 1195-1210.
Tsao, A., Moser, M.B., and Moser, E.I. (2013). Traces of experience in the lateral entorhinal cortex. Curr Biol 23, 399-405.

Tulving, E., Le Voi, M.E., Routh, D.A., and Loftus, E. (1983). Ecphoric processes in episodic memory. Philos Trans R Soc Lond B Biol Sci 302, 361-371.
van Dijk, M.T., and Fenton, A.A. (2018). On How the Dentate Gyrus Contributes to Memory Discrimination. Neuron 98, 832-845.
Vinck, M., Oostenveld, R., van Wingerden, M., Battaglia, F., and Pennartz, C.M. (2011). An improved index of phase-synchronization for electrophysiological data in the presence of volume-conduction, noise and sample-size bias. Neuroimage 55, 1548-1565.
Wang, C., Chen, X., Lee, H., Deshmukh, S.S., Yoganarasimha, D., Savelli, F., and Knierim, J.J. (2018). Egocentric coding of external items in the lateral entorhinal cortex. Science 362, 945-949.
Whittington, M.A., Traub, R.D., and Jefferys, J.G. (1995). Synchronized oscillations in interneuron networks driven by metabotropic glutamate receptor activation. Nature 373, 612-615.
Wu, C.T., Haggerty, D., Kemere, C., and Ji, D. (2017). Hippocampal awake replay in fear memory retrieval. Nat Neurosci 20, 571-580.
Ye, J., Witter, M.P., Moser, M.B., and Moser, E.I. (2018). Entorhinal fast-spiking speed cells project to the hippocampus. Proc Natl Acad Sci U S A 115, E1627-E1636.

STAR Methods

Subjects

A total of 12 wild-type mice with a mixed C57BL6/FVB background were used for the study. The mice were 3 - 6 months old during surgery. Nine mice were implanted with linear silicon arrays. Three mice were implanted with a metal head plate for head-fixed recording using linear silicon arrays and Neuropixel probes (Jun et al., 2017).

Surgery

LFP recordings were collected using 32-channel (8 mice) and 16-channel (1 mouse) linear silicon array electrodes (Neuronexus, Ann Arbor, MI) with 50 µm spacing and 703 um^2 electrode area. 32-channel electrodes spanned both CA1 and DG locations, and the 16-channel electrode spanned only DG locations. The electrodes were implanted stereotaxically under isoflurane anesthesia (2%, 1 L/min). The tip was aimed at -1.85 AP, ±1.20 ML, -2.3 DV relative to bregma. The electrodes spanned the dorso-ventral axis of the dorsal hippocampus. Reference electrodes were aimed at the cerebellar white matter. The electrode assemblies were anchored to the skull using 3-4 bone screws with dental cement (Grip Cement, Dentsply, Milford DE). One anterior screw was used as a ground. A four-wire stimulating electrode bundle was made by twisting together four 75-µm diameter nichrome wires (California Fine Wire, Grover Beach, CA). The bundle was cut at an angle so as to span 0.5 mm. During surgery, the stimulating bundle was placed in the ipsilateral perforant path +0.5 AP, ±4.1 ML, 1.0-1.6 DV from lambda. Evoked response waveforms were carefully checked with different pair combinations of stimulation electrode channels. In the mice that were used for head-fixed recordings, a titanium head plate was attached to the skull using dental cement and the exposed skull was covered with KwikSil, a low toxicity adhesive (World Precision Instruments, Sarasota, FL) and protected with an attached plastic cup. All mice were allowed at least 1 week to recover. In mice that were used for head-fixed recordings, a secondary surgery was performed immediately before the

experiment. The plastic cap and KwikSil was removed and a skull opening to enable electrode placement was drilled at 1.85 AP, ±1.20 ML relative to bregma. Between consecutive days of recordings, a KwilSil-protective cup assembly was reattached to prevent infection.

Electrophysiology recording

An amplifier board with 32 unipolar inputs and 3-axis accelerometer (RHD2132, Intan Technologies, Los Angeles, CA) was connected directly to the Neuronexus probe for signal amplification and digitization. A lightweight, counter-balanced cable (Intan Technologies, Los Angeles, CA) was used to power the amplifier board and the infrared LED used for tracking as well as to transmit digital data to the computer using a custom recording system connected to the USB port of a PC. The cable was connected through a lightweight commutator to enable free movement of the animal. The signal from each electrode was low-pass filtered (500 Hz) and digitized at 2 kHz. Evoked responses were obtained using a constant current stimulus isolation unit (WPI, Sarasota, FL; model: A365RC) that was used to deliver individual unipolar 100 μs stimulus pulses across the electrode pair. Evoked responses were low-pass filtered at 4 kHz and sampled at 8.12 kHz. In head-fixed recordings, the signal from a Neuropixels probe was filtered between 0.5 Hz and 1 kHz and sampled at 2.5 kHz for LFP recordings and filtered between 300 Hz and 10 kHz and sampled at 30 kHz for single unit recording. Both electrophysiology systems were synchronized using square TTL pulses generated by the Neuropixels system that was recorded by both systems. The animals were recorded during a 30-minute session in their homecage during the first exposure to the experimental room. The mouse's movements during recordings was monitored continuously using a video tracking system (Tracker, Bio-Signal Group, Acton, MA) that was synchronized to the electrophysiology data using the video frame pulses generated by the camera.

Data Analysis

LFP and electrode localization

LFPs were localized by visual LFP inspection of sharp-wave ripples in CA1 *stratum pyramidale* and dentate spikes in the hilus of the dentate gyrus (Fig. S1). Electrode locations were verified histologically at the end of recordings (Fig. S2). In the mouse implanted with the 16-ch electrode array, only dentate LFPs were recorded because of the limited spatial span of the electrode.

Detection and classification of dentate spikes

The LFP channel with the largest visually identified amplitude of dentate spike was band-pass filtered 5-100 Hz and the amplitude was z-score normalized. Next, all local peaks in the band-pass signal were detected, and several features were extracted. Specifically, the features included the amplitude difference between the DS maxima and the preceding as well as following minima, and also the spike width that was measured at the level of either the preceding or following minima, whichever was closer to the maxima. The spike amplitude distributions were further normalized by z-score normalization of the log-transformed amplitudes. Putative dentate spikes were selected if the amplitudes compared to the preceding and following minima were > 0.75 and when the width of the event was between 5 and 25 ms. The optimal values were selected based on analysis of the feature histograms.

Dentate spikes were classified as DS_L and DS_M based on their CSD profiles. CSDs were calculated using the CSDplotter Matlab toolbox (Pettersen et al., 2006) at the peak of a putative DS event. Independently for each recording, the CSD for each putative DS event was analyzed for local minima, corresponding to CSD sinks (Fig. 2A). The histogram of detected local minima of all putative DS events was plotted and the local maxima that represented the highest probability of current sinks were manually identified (color dots in Fig. 2A, middle). This analysis resulted in 4 locations corresponding to (from top to bottom) the outer molecular layer of the

suprapyramidal DG blade (supraDG), the middle molecular layer of supraDG, middle molecular layer of the infrapyramidal DG blade (infraDG) and the outer molecular layer of infraDG. DS_L and DS_M were then identified separately from the supraDG and infraDG molecular layers as putative DS events with a sink occurring ± 25 μm around the location selected in the sink histogram. DS events classified using sinks in the molecular layer of supraDG were used throughout the study, although the results did not change when classification from infraDG was used instead.

Detection of ripple events

We followed a previously published algorithm (Csicsvari et al., 1999) with several modifications to detect ripple events. We used the LFP recorded from the CA1 *stratum pyramidale* electrode, where ripples were identified visually. First, the signal was 150-300 Hz band-pass filtered. Next, we computed the sliding root-mean square (RMS) estimate in a 10-ms window. Next, we z-scored normalized the RMS estimate and detected local maxima with $z > 3$. Finally, for each detected event, we computed the wavelet time-frequency representation of the LFP and for each detected event we extracted its frequency as a local peak in the time-frequency wavelet spectrum. Only events with frequencies between 130-250 Hz were selected for further analysis.

Independent components analysis of the LFP

We used independent component analysis (ICA) to extract the specific CA1 dendritic components (Fernandez-Ruiz and Herreras, 2013; Fernandez-Ruiz et al., 2017), which minimizes the impact of volume conducted signals and estimates the components that can be precisely matched to specific dendritic compartments. LFP signals that were recorded using linear silicon array electrodes were decomposed into individual dendritic components using a previously described procedure (Fernandez-Ruiz and Herreras, 2013; Fernandez-Ruiz et al., 2017; Makarov et al., 2010) with several modifications. First, LFP signals were filtered between 20 Hz and 150 Hz. Next, principal component analysis (PCA) was applied to the filtered LFP

data in order to find how many principal components explain over 99% of the signal variance in the data. Next, independent component analysis (ICA) was applied to the filtered LFP data using the FastICA Matlab toolbox (Hyvarinen, 1999) by specifying number of principal components that were obtained in the previous steps for both PCA-based dimensionality reduction and the target number of resulting independent components. Next, components of the unmixing matrix were used to compute CSDs of the individual voltage loadings for component localization and independent components (ICs) were processed using comodulogram analysis for frequency-based classification of components. Here, we took advantage of theta phase coupling of gamma oscillations, which can reveal a specific frequency footprint of each component (Schomburg et al., 2014). Specifically, the LFP from the *stratum pyramidale* electrode was filtered using set of FIR filters with 2 Hz bandwidth, in the range 5-11 Hz followed by the Hilbert transform to obtain the phase of CA1 theta oscillations. Next, independent components were filtered using 20 Hz wide filters in the range 20-150 Hz followed by the Hilbert transform to obtain amplitude information from individual components. Details of the filters and filtering procedure were described previously (Dvorak and Fenton, 2014). The phase and amplitude information were then combined between all pairs of frequency bands used to obtain phase and amplitude information and a modulation index (Tort et al., 2010) was computed for each pair resulting in a comodulogram (Figs. 3D) that reveals the peak coupling between the phase of theta and the amplitude of a given IC. We found that the ICA analysis provides better segregation of the independent components if the number of LFP channels is restricted before applying ICA. On the other hand, it is not possible to say which LFP channels to include in the analysis for best IC separation. Consequently, we performed a grid search, where we systematically repeated ICA for different numbers of included contiguous segments of LFP channels referenced either to *stratum pyramidale* for CA1 (Fig. 3) or to the *hilus* for DG (Fig. 5). The resulting CSD profiles of ICs were then visually compared and selected based on both the CSD profile of voltage loadings and a clearly isolated peak of coupling between theta phase and

the amplitude of a given component. While this operation is extremely computationally intensive, it allowed robust detection of the corresponding components in all the mice we studied (Fig. S3).

Phase locking analysis

To study the phase coupling between different oscillatory rhythms, we used the phase locking value (PLV) estimate (Lachaux et al., 1999), which provides a good estimate of phase locking for signals where the volume conducted signals have been minimized by ICA (Vinck et al., 2011). To calculate PLV of a pair of signals, we used an array of complex Morlet wavelets spaced by 1Hz between 20 Hz and 100 Hz convolved with each of the ICs in the pair to obtain the instantaneous phase of both ICs at a given frequency. Next, we computed the instantaneous phase difference between the two ICs, IC_1 and IC_2. Then, for all pairs of time offsets in the range -100 ms to +100 ms relative to the DS event and each frequency, we computed instantaneous phase differences across all DS events $\Delta\varphi(t,f) = \varphi_1(t,f) - \varphi_2(t,f)$. Finally, we computed PLV across DS events as $PLV = \frac{1}{N}\left|\sum_{n=1}^{N} exp\big(i \cdot \Delta\varphi(t,f)\big)\right|$, where i is the imaginary unit, N is number of DS events, t is the offset relative to DS event and f is frequency used to filter signal to obtain its phase. Repeating this algorithm for a range of frequencies and offsets relative to DS events generates a time-frequency PLV estimate that is centered at each type of DS (Fig. 5B).

Detection of oscillatory events

A published algorithm was used to extract oscillatory events from the LFP (Dvorak et al., 2018). In the first step of the algorithm the LFP is transformed into a time-frequency power representation by convolving the LFP signal with a group of complex Morlet wavelets resulting in complex band-specific representations across a specific frequency range. Instantaneous normalized power was then obtained by squaring the argument of the band-specific signal representation and dividing it by the square of the standard deviation of the band-specific signal.

Next, oscillatory events were detected as local 2-D peaks in the normalized time-frequency space with z-scored power > 2.5. Such peaks were then localized both in time and frequency.

Detection of oscillatory cycle minima

To detect the oscillatory cycle minima of individual oscillations (Fig. 4), we started by correcting the polarity of ICs, because the polarity of individual ICs is arbitrary (Hyvarinen, 1999). Here, we took the advantage of known relationship between hippocampal gamma oscillations < 100 Hz and spectral leakage of spiking activity (Fig. S4), that can be observed > 150 Hz at *stratum pyramidale* (Dvorak and Fenton, 2014; Lasztoczi and Klausberger, 2016; Schomburg et al., 2012). We first created a set of Morlet wavelets covering 20-50 Hz for *sr* ICs or covering 60-90 Hz for *slm* ICs and used them to obtain the instantaneous phase of IC components at specific frequencies. Next, we filtered the LFP from *stratum pyramidale* in the frequency range 150-250 Hz followed by a Hilbert transform to obtain the amplitude of the high frequency activity that served as a proxy for spiking activity. Next, for each IC, we created a phase-amplitude histogram of 150-250 Hz amplitude distribution relative to the phase of IC component either in the 20-50 Hz range or the 60-90 Hz range (Fig. S4B). Finally, we visually compared the resulting relationships and corrected each component so that the 150-250 Hz spiking-proxy activity was maximal at the descending phase of the *sr* IC close to the trough and the ascending phase of *slm* IC close to the trough (Fig. S4C). This step allowed us to reliably correct the polarity of all components from all animals in order to compare the modulation of oscillatory cycles relative to DS across the entire dataset. After correcting the polarity of IC components, we detected individual oscillations (Fig. 1B) using time-frequency decomposition and detection of power peaks as described earlier and then detecting local minima in ± 50 ms window around oscillatory peak in *sr* IC and ± 29 ms window around oscillatory peak in *slm* IC corresponding to 3 cycles of oscillatory activity centered at strongest oscillatory cycle minima close to detected

oscillatory peak (Fig. S4D, E). The timestamps of individual cycle minima were recorded and used for later processing.

Single unit analysis

Single units were sorted using published open-source algorithm Kilosort2 (Pachitariu et al., 2016) that is optimized for Neuropixels probes and takes advantage of GPU processing to improve algorithm performance. After automated clustering of the data, we selected only units with < 20% estimated contamination rate with spikes from other neurons that were computed from the refractory period violations relative to expected. We also excluded units with non-characteristic or noisy waveforms resulting in identifying a total of 9404 single units.

The units were then localized to neocortex, CA1, DG/CA3 and thalamus using three criteria: 1) the depth of the Neuropixel probe relative to the cortical surface, 2) localization of dentate spikes in the hilus of dentate gyrus and sharp wave ripples in CA1 *stratum pyramidale* and clustering of units along the depth of the linear Neuropixel array. The clustering of units into different regions becomes apparent when we plot the depth of the maximal amplitude of the average action potential waveform for each unit along the length of the probe (Fig. S6A). The cluster of single units that overlaps with the detected location of sharp-wave ripples was classified as CA1, whereas the cluster of units that overlaps with the detected location of DS was classified as DG/CA3. The cluster of units between CA1 and the cortical surface was classified as neocortical neurons and the large amplitude units below DG/CA3 were classified as thalamic neurons. To separate CA3 from DG units, we used two additional criteria. First, we used the anatomical location, confirmed by histology, and considered CA3 units to only be from electrodes that were more lateral than +1.5 mm relative to bregma. Second, we took advantage of the asymmetric profile of the perforant path termination in DG that is apparent in the CSD profiles of LFPs that were recorded with Neuropixel probes and triggered by DS_M events (Fig. 7B). ECII projections to the infraDG terminate at the mediolateral extent at which CA3 begins,

while ECII projections to the supraDG continue in parallel with CA3 (Fig. 7B; Fig. S2). Electrodes that exhibited only a dorsal current sink were classified as CA3, while electrodes that exhibited a symmetrical pair of current sinks were classified as DG. To further classify DG cells as putative granule cells (GC) and mossy cells (MC) we took advantage of two identified locations, that of the granule cell layer at the CSD reversal between the current sink in the middle molecular layer and the current source in the hilus triggered by DS_M, and that of the maximal amplitude of the average action potential of a given cell. Cells within 150 μm of the CSD reversal were classified as GC, while cells deeper than 150 μm were classified as MC (Senzai and Buzsaki, 2017). This procedure resulted in localizing 1413 cells to neocortex, 6422 neurons to thalamus, 492 cells localized to CA1, 696 cells localized to DG and 285 cells localized to CA3.

To classify units into putative excitatory and inhibitory neurons we used a similar approach as in other studies (Jia et al., 2019; Senzai and Buzsaki, 2017; Talbot et al., 2018a) and extracted several features associated with the average action potential waveshape and features associated with firing properties (Fig. S6). Datasets were split into DG cells and CA1 + CA3 cells and the two datasets were independently analyzed using the k-Means algorithm implemented in JMP 14 software to identify three clusters corresponding to three types of neurons classified as principal cells (E), narrow-waveform interneurons (In) and wide-waveform interneurons (Iw). In the analyses that follow, we only focus on E and In cells because of their maximal separation in the feature space.

Peri-DS-event time cofiring histogram

We assessed the probability that a pair of cells would co-fire relative to the occurrence of a dentate spike by computing a cofiring probability for each cell pair. The probability was computed in a 6 ms-long window centered on the dentate spike peak. The co-firing probability

was compared to randomly sampled events to obtain a ratio of co-firing change. Statistical validation was computed using a t test between the co-firing probabilities during DS events and randomly sampled times that were normalized by the marginal discharge probabilities of both cells to account for increased firing rate changes during DS. The significance threshold was corrected using Bonferroni's method. See Supplemental Information for details.

Statistical analyses were performed using JMP version 14 (SAS, Cary, NC) and Matlab 2019b (Mathworks, Natick, MA). Significance was accepted at $p < 0.05$. Exact p values are reported throughout.